An MRI-Compatible Needle Manipulator Concept Based on Elastically Averaged Dielectric Elastomer Actuators for Prostate Cancer Treatment: An Accuracy and MR-compatibility Evaluation in Phantoms

Jean-Sébastien Plante, Kenjiro Tadakuma, Lauren M. DeVita, Daniel F. Kacher, Joseph R. Roebuck, Simon P. DiMaio, Ferenc A. Jolesz, Steven Dubowsky

- J.S. Plante: Département de génie mécanique, Université de Sherbrooke, Sherbrooke, Québec, JIK 2R1, Canada, Tel: (819) 821-7144, FAX: (819) 821-7163, jean-sebastien.plante@usherbrooke.ca,

- K. Tadakuma, L.M. DeVita and S. Dubowsky: Mechanical Engineering Department, Massachusetts Institute of technology, 77 Massachusetts Ave., Cambridge, MA, 02139, Tel: (617) 253-2144, FAX: (617) 258-7881, dubowsky@mit.edu.

- D.F. Kacher, J.R. Roebuck, S.P. DiMaio and F.A. Jolesz: Division of MRI and Image Guided Therapy Program Department of Radiology Brigham and Women's Hospital Harvard Medical School, 75 Francis Street, Boston, MA, 02115, Tel: (617) 732-5961, FAX: (617) 582-6033, jolesz@bwh.harvard.edu

ABSTRACT

Background. A parallel manipulator concept using bistable polymer actuators has been developed to perform prostate cancer biopsy and deliver therapy within the bore of a Magnetic Resonance Imaging (MRI) scanner. The dielectric elastomer actuators (DEA) used in this manipulator concept are promising for MRI-compatible robotics because they do not interfere with the high magnetic fields of MRI while having good mechanical performance and being low cost. In the past, these actuators have been plagued by robustness problems when used in a continuous manner. Recent studies show that reliability significantly improves when DEAs are used in a bistable manner such as proposed here.

Method of Approach. This paper investigates the potential of the proposed manipulator concept by evaluating the positioning accuracy and MRI-compatibility of a laboratory prototype developed for clinically relevant design criteria.

Results. An analytical model of the manipulator kinematics is presented. Analytical and experimental results validate that the proposed technology can provide accurate needle placement required to perform prostate cancer treatments. The prototype's MRI compatibility is validated in a 3 Tesla clinical MRI scanner.

Conclusions. The parallel manipulator concept using bistable polymer actuators is shown to be a viable approach to perform MRI-guided needle insertions for prostate cancer biopsy and therapy.

Keywords: MRI-compatible robot, binary robotics, dielectric elastomer actuator, parallel manipulator, prostate cancer.

1. INTRODUCTION

A parallel manipulator for Magnetic Resonance Imaging (MRI) guided prostate cancer biopsy and therapy has been developed (Fig. 1). The manipulator is a binary mechatronic system that departs from conventional continuous approaches. Binary systems have been proposed to overcome the limitations of conventional continuous systems for applications including space exploration systems and medical devices [1,2,3]. Binary systems are driven by actuators that switch between two stable states. These systems are simple, do not use power to hold their state, and require fewer sensors than traditional systems [4]. However, the lack of practical binary actuators has been a major limitation in the past.

Recent advances have made Dielectric Elastomer Actuators (DEAs) an effective and practical solution to this problem [5]. They are lightweight, simple, inexpensive, and virtually all plastic. It has been shown that using DEAs in a bistable manner, intermittently and at high speeds, avoids the reliability problems that have plagued them when used in a conventional, continuous fashion. [6]. Figure 2 shows the bistable actuators used in this study. They consist of an antagonistic pair of DEAs that switch a bistable element between two stable positions. Furthermore, unlike most conventional actuators, previous experiments

with DEAs showed these actuators to be MRI-compatible, meaning that they do not react or interfere with the high magnetic fields of MRI nor impact image quality [7,8].

Unlike conventional robotic systems using one high resolution continuous actuator per degree-of-freedom (DOF) to achieve good accuracy, parallel bistable manipulators use many low resolution actuators with only two available positions per DOF. This results in an overconstrained system. Compliance can be used to accommodate for this overconstraint using elastic averaging where the compliance of the system mediates between the bistable actuators to achieve high accuracy positioning [9]. The overconstrained parallel architecture can lead to compact and relatively stiff systems compared to conventional serial chain approaches. Hence, elastically averaged parallel manipulators based on DEAs are proposed as a method to develop MRI-compatible robotic and mechatronic systems [2].

Prostate cancer treatment is a highly relevant application for the proposed parallel manipulation technology using bistable DEAs. Prostate cancer is the most common non-cutaneous cancer and the second most common cause of all cancer related deaths in men [10]. In the United States alone, 218,890 men were diagnosed with prostate cancer in 2007 and about 30,000 men die from the disease each year [10,11]. Prostate cancer engenders large societal and economic costs, averaging $12,000 after six months of treatment [12]. The range of available treatment options for prostate cancer could benefit by using MRI-compatible robotic manipulation as it allows operators to target sub-centimeter regions using the optimal soft tissue conspicuity of MRI, potentially more safely and more effectively than is currently possible. Indeed, manually performed MRI-guided interventions have already shown great promise and the addition of robotic manipulators would further advance the field [13].

The objective of this paper is to evaluate the potential of the proposed parallel manipulator concept using bistable DEAs with respect to the fundamental issues of positioning accuracy and MRI compatibility. Practical issues such as sterilization and manipulator control are beyond the scope of the paper. Here, a brief review of prostate cancer therapies is conducted. The proposed manipulator system is presented along with an analytical model of its kinematics. Model predictions compared with experimental results show that, with proper manufacturing techniques, the manipulator system could meet the clinically mandated targeting accuracy. Finally, the prototype is shown to be MRI safe and compatible with a 3 Tesla MRI scanner. The proposed manipulator concept is shown to be promising for applications with MRI-guided biopsy and therapy.

2. BACKGROUND AND MOTIVATION

Needle biopsy is a tool used in the diagnosis of prostate cancer, in which a needle is inserted into the prostate and small specimens of tissue are removed for histological analysis. After the diagnosis is made, a malignant tumor can be treated using several options including surgery (e.g., robot-assisted or open radical or nerve sparing prostatectomy), radiation therapy (e.g., external beam radiotherapy or brachytherapy), or pharmacotherapy (e.g., adjuvant chemotherapy). ”Watchful waiting” is often the preferred option in more indolent cases when surveillance using regular blood tests and as-needed follow up imaging is employed. Brachytherapy is a form of radiation therapy where multiple tiny radioactive “seeds” are implanted into the prostate tumor using needles to target each of the cancer foci identified in the treatment plan (Fig. 3) [14]. There are two approaches to reach a target within the prostate using a needle: transrectal and transperineal. The transperineal approach (Fig. 3), entails placing a template of regularly spaced needle guide holes against the perineum and carries a much lower risk of infection than does introducing the needles via the rectal wall into the prostate.

Image-guidance is necessary to facilitate tumor localization and needle targeting for both prostate biopsy and brachytherapy. Ultrasound-guided transperineal brachytherapy is growing in popularity over other treatment options at many centers because it is an outpatient procedure with high success rates, significantly smaller chance of incontinence and impotence, and quick treatment and recovery [14]. MR-guidance and more specifically T2-weighted MRI performed at high field strength, provides superior conspicuity of prostate cancer foci regardless of the approach employed for needle targeting. Thus MRI-guidance using the transperineal approach could be employed to both improve conspicuity compared to US-guidance and to lower infection rates compared to the transrectal approach [15,16]. High field MRI (i.e., 3 Tesla) is also likely to allow smaller lesions to be visualized than can be currently be detected using ultrasound. Thus MRI-guidance using the transperineal approach and high field strength scanners could be used to detect multicentric disease, a common finding in most prostate cancer patients, thereby facilitating maximally effective biopsy and brachytherapy seed placement.

Considerable work on the development of targeting systems for cylindrical closed bore MRI-guided procedures has been presented for prostate interventions [17,18,19,20,21,22,23,24,25,26] breast interventions [27], abdomen and spine interventions [28] as well as general purpose robots [29]. Although vertically open MRI scanners [30,31,32] offer greater patient access, the earlier pioneering work with these scanners will become relevant only if such scanners are again made commercially available, and moreover at higher field strengths to overcome previous limits in image quality attending the low field strength.

The impact of materials and electronic devices on MR image quality must be considered [33,34,35]. Materials with high susceptibility disrupt the homogeneity of the magnetic field, resulting in image

distortion and signal dropout. Electromagnetic interference from active devices can increase the noise in the image or create narrow bands of noise (zipper artifact). A device not exhibiting attraction or torque in the magnetic field, not impacting image quality, and operating without impairment in the magnetic field can be considered MRI safe and compatible.

Some efforts have assured MRI compatibility by eliminating actuation in favor of manual manipulation of an assist device [17,18,19]. This approach requires access to the patient that can be afforded by removing him from the bore of the scanner. A limitation, however, is that realtime image guidance cannot be utilized to monitor needle deflection nor shifting of the anatomy inherent to needle insertion [36]. In order to take full advantage of real time image guidance to correct or steer [37] the needle trajectory and target difficult locations, fully actuated assist devices are ideal because they do not require the removal of the patient from the bore of the scanner, which potentially translates into shorter and safer procedures.

The high magnetic fields of closed-bore MRI scanners require actuators with more demanding MRI compatibility. Piezoelectric and pneumatic actuators are a logical solutions for MRI-compatible robots. However, even if piezoelectric actuators have been successfully tested in a 0.7 Tesla open-bore MRI [38], there have been reports of image distortion when used at higher fields such as inside the bore of a 1.5 Tesla scanner [39]. Systems using pneumatic cylinders are difficult to control because of their inherent imprecision and compliance [40,41]. Pneumatic stepper motors have recently been proposed to eliminate the controllability problem [42]. However, both piezoelectric and pneumatic actuators generally lead to relatively complex and expensive systems.

DEAs have a unique potential for MRI-compatible robots compared to piezoelectric and pneumatic actuators. They offer excellent MRI compatibility [7,8], have good mechanical performance and reliability when used in a bistable manner such as proposed here, and are inherently simple and low cost.

3. PROPOSED MANIPULATOR

3.1 Design Requirements

The following design requirements were established with input from practicing radiologists familiar with MRI-guided interventions to focus the design of the manipulator prototype. The geometric constraint for positioning the device is dependent of patient habitus. The workspace was established using a set of foam cast legs/pelvis placed inside the bore of a 60 cm MRI scanner.

A. System overall dimensions: The device must fit between a patient's legs while he is lying supine inside a closed-bore MRI system. The device must fit inside a work envelope of 20cm in diameter by 50cm deep, placed about 20-30cm from the perineum (Fig. 4a). The needle is guided by a needle guide tube that extends between the device and the prostate. Needles could either be back or front loaded.

B. Positioning accuracy: The positioning accuracy is defined as the average distance from a random point to the nearest possible end effector point in the entire workspace. Our goal is to double the positioning accuracy achievable using the current manual insertion techniques with perforated templates with holes 5mm apart (Fig. 3). As the average distance from a random point to a 5mm x 5mm grid is 1.9mm, the positioning accuracy design specification for our prototype is set to 1mm.

C. Workspace dimensions: The required workspace to accommodate an enlarged prostate as seen in some patients is an 80mm x 70mm ellipse extruded 70mm deep (Fig. 4b). The workspace is located 60mm deep under the skin. Hence the needle must penetrate between 60 and 130mm in the z-direction.

D. Insertion forces: The maximum needle penetration force specification of 14N and maximum force perpendicular the needle of 1.6N were set based on animal muscle tissue tests and values from the published literature [43].

3.2 Proposed System Description and Operation

The system is a parallel manipulator that has two planes, each with six bistable actuator elements symmetrically distributed around a radius. Its kinematic configuration is shown in Figs. 1 and 5. Each actuator can be independently activated to a predetermined extension. The surgical needle runs through a tube at the nominal center of each actuator plane and advances from plane 1, through plane 2 (labeled p1 and p2, respectively, in Fig. 5b) to the target. The needle would be driven in the tube by an insertion module using DEAs that has yet to be developed. Each bistable actuator assembly is attached to the center of the plane by springs with different spring constants, as discussed in Section 5. The bistable assembly is composed of two antagonistic cone-shaped actuators that switch a bistable structure to one of two positions (Fig. 2). Figure 5 shows all bistable assemblies in the “off” position. When switched to the “on” position, the bistable devices will move radially inward by a fixed amount. The manipulator requires minimal electronic hardware that would be mounted in the MRI room at a safe distance from the magnet. The device is intended to be operated in “open loop” mode with visual feedback of the operator using real-time images. The control of binary parallel manipulators remains to be studied and is beyond the scope of the paper.

4. MANIPULATOR ANALYTICAL MODEL

A binary system can only reach a finite set of discrete points. A fine positioning accuracy is achieved by using many redundant bistable modules per output DOF. Here, 12 bistable modules control the 2 DOF of the needle tip (x-y position). An analytical model of the resulting overconstrained system is developed by analyzing each plane of the device.

Each plane of the system has six nodes joining the springs and the bistable modules (Fig. 5). The nodes motions are imposed by the extended or retracted states of the bistable modules. The system's binary inputs, Q, can thus be defined by:

$$Q = [a_1, a_2, ..., a_i, ..., a_n] \qquad (1)$$

where n is the number of modules and $a_i (i = 1, 2, ..., n) = 1$ or 0 takes the values of 1 or 0 to represent the extended or retracted state of the ith bistable module.

The deformations of the springs due to the motion of nodes 1 to n and to the presence of external forces are shown in Fig. 6 (Not all of the variables described below are shown for clarity). A closed-loop position constraint equation is written in the *O-xy* coordinate system as:

$$\mathbf{l}_i = \mathbf{l}_{si} - \mathbf{U} \qquad (2)$$

where:

- $\mathbf{l}_i$ is the position vector of the ith undeformed spring as defined by $\mathbf{l}_i = \overrightarrow{O'A_i} = l_i \mathbf{v}_i$ with $\mathbf{v}_i = \{\cos\varphi_i, \sin\varphi_i\}^T$ the unit vector of $\mathbf{l}_i$ and φ_i is the orientation angle of $\mathbf{l}_i$.
- $\mathbf{l}_{si}$ is the position vector of the ith deformed spring as defined by $\mathbf{l}_{si} = \overrightarrow{OA_i} = (l_{oi} + \delta_i)\mathbf{w}_i$ with:
    - l_{oi} the undeformed length of the ith spring.

- $\delta_i = \Delta_i + a_i\xi_i$ the stretched length of the *i*th spring along the axis of *i*th undeformed spring where Δ_i is the pre-stretching length and ξ_i is the stroke of *i*th actuator.
- $\mathbf{w}_i$ the unit vector of the *i*th spring along the *i*th undeformed spring as defined by $\mathbf{w}_i = \{\cos\theta_i, \sin\theta_i\}^T$ with θ_i the position angle of the *i*th undeformed spring.

- $\mathbf{U}$ is the vector displacement of the center point as defined by $\mathbf{U} = \overrightarrow{OO'} = U\mathbf{e}'$ with $\mathbf{e}' = \{\cos\phi, \sin\phi\}^T$ the unit vector of $\mathbf{U}$ and ϕ is the orientation angle of $\mathbf{U}$.

Equation (2) can now be written as:

$$l_i\mathbf{v}_i = (l_{oi} + \Delta_i + a_i\xi_i)\mathbf{w}_i - U\mathbf{e}' \qquad (3)$$

The deformation of the *i*th spring along axis of the *i*th deformed spring is:

$$\dot{\delta}_i\mathbf{v}_i = (\dot{l}_i - \dot{l}_{0i})\mathbf{v}_i = (\dot{l}_{oi} + \dot{\Delta}_i + a_i\dot{\xi}_i)\mathbf{w}_i - \dot{U}\mathbf{e}' - \dot{l}_{0i}\mathbf{v}_i, \quad i = 1,2,...,n. \qquad (4)$$

and the internal force of the *i*th actuator is:

$$\mathbf{F}_i = -k_i\dot{\delta}_i\mathbf{v}_i = -k_i[(\dot{l}_{oi} + \dot{\Delta}_i + a_i\dot{\xi}_i)\mathbf{w}_i - \dot{U}\mathbf{e}' - \dot{l}_{0i}\mathbf{v}_i], \quad i = 1,2,...,n. \qquad (5)$$

where k_i is the stiffness of the *i*th spring.

Static equilibrium in the plane requires that the sum of the forces at the center point to be zero:

$$\sum\mathbf{F} = \sum_i \mathbf{F}_i + \mathbf{f}_{ext} + \mathbf{W} = \mathbf{0} \qquad (6)$$

where $\mathbf{f}_{ext}$ and $\mathbf{W}$ are the external force vector and weight vector at center point, respectively.

The workspace of each plane of the system can be obtained by solving Eqs. (5) and (6) iteratively. The locations $\mathbf{X}_d$ (x_{dm}, y_{dm}, z_{dm}) of the end effector of the manipulator (needle tip) are calculated from:

$$\mathbf{X}_d = \mathbf{U}_1 + \frac{z_{dm}}{p}\left(\mathbf{U}_2 - \mathbf{U}_1\right) \qquad (8)$$

where $\mathbf{U}_1(x_1, y_1, 0)$ and $\mathbf{U}_2(x_2, y_2, p)$ are the workspace of the two parallel planes, p is the distance between the planes, and the origin is taken as the center point of p_1 before any perturbation.

Neglecting the effects of external forces $\mathbf{f}_{ext}$ and **W,** the position of the central point can be obtained from Eqs. (5) and (6) as:

$$U\mathbf{e}' = \frac{1}{\sum_i k_i}\sum_i k_i[(l_{oi} + \Delta_i + a_i\xi_i)\mathbf{w}_i - l_{0i}\mathbf{v}_i] \qquad (9)$$

Defining a dimensionless stiffness as the ratios of stiffness springs, $\mu_i = k_i / k_1$, yields:

$$U\mathbf{e}' = \frac{1}{\sum_i \mu_i}\sum_i \mu_i[(l_{oi} + \Delta_i + a_i\xi_i)\mathbf{w}_i - l_{0i}\mathbf{v}_i] \qquad (10)$$

Equation (10) shows that when there are no external forces, the output displacements of the plane actuation are functions of the ratio of interconnecting spring constants, and not the constants themselves. Equations (8) and (10) show that the workspace of the manipulator, and thus its accuracy, can be optimized by properly selecting the ratios of spring stiffness and the distance between the two planes of actuation modules.

The system's ability to resist disturbance forces is quantified by its effective stiffness at the needle tip:

$$K_{eq,tip} = \frac{k_{eq1}k_{eq2}p^2}{k_{eq1}\left(p + \zeta\right)^2 + k_{eq2}\zeta^2} \qquad (11)$$

where p is the distance between the planes and ζ is the distance from the second actuator plane to the prostate. k_{eq1} and k_{eq2} are the equivalent stiffness at connected points in the actuation modules. The equivalent stiffness in the plane actuation modules can be written as:

$$\begin{bmatrix} k_{eqx} \\ k_{eqy} \end{bmatrix} = \sum_i \begin{bmatrix} k_i |\cos\varphi_i| \\ k_i |\sin\varphi_i| \end{bmatrix} \qquad (12)$$

5. ANALYTICAL RESULTS

The above analytical model is used with the parameters listed in Tables I to III to predict the performance of the experimental manipulator.

Figure 7a shows the needle workspace at penetrations from 60 to 130mm. Figure 7b shows the cross section of the workspace at a penetration of 110mm. The system design covers the required workspace quite well. A binary system's accuracy is determined by its configuration and the number of actuators. This system with 12 binary actuators can reach 4096 (2^{12}) points. In general, these points will not be distinct or uniformly distributed over the workspace. Here, the actuator springs are chosen to have different spring rates to eliminate system symmetries resulting in nondistinct points.

To evaluate the model predicted positioning accuracy, 1000 random target points within the workspace were chosen and the minimum distance from the closest possible end effector to each of these points was calculated. Note that model predicted positioning accuracy does not account for the effects of manufacturing tolerances, needle deflection due to tissue interaction, and trajectory corrections made by the operator during insertion. Figure 8 shows the distribution of the minimum distances from a reachable end effector point to a randomly selected target location. The average distance and standard deviation, for a random point to the nearest possible end effector point in the entire workspace are 0.68mm and

0.51mm, respectively. The same values for a workspace the size of a prostate are 0.41 mm and 0.21 mm. Clearly, the model predicted accuracy meets the design requirement of an average distance of 1 mm.

Figure 9 shows the distribution of system stiffness in the radial direction at points located at a depth of 110mm from the perineum. The values in the other directions perpendicular to the needle are similar. Figure 9 shows that the stiffness of the system is quite uniform. The radial stiffness for any point in the workspace is within 10% of the average stiffness of the system. As shown by Eq.(10) above, changing the spring stiffness of each spring while maintaining the spring stiffness ratios between the springs does not affect the workspace. For example, doubling all spring constants would double the system stiffness without changing the workspace. However, for a given actuator extension, the spring constants are limited by the maximum actuator forces.

6. EXPERIMENTAL SYSTEM DESCRIPTION

An experimental laboratory prototype (Fig. 1b) was fabricated and tested according to the parameters listed in Tables I to III. The system has 12 functional bistable modules, each using two cone-shaped DEAs. The cone actuators used in this study have 2 layers of polymer (VHB 4905, 3M Worldwide, St Paul, MN, 1.5mm initial thickness). Current hand fabrication techniques limit the number of film layers and thus actuator force. Consequently, overall system stiffness is very low due to the low spring rates used to prevent saturation of the hand-fabricated actuators. It is estimated that actuators with 30 to 50 layers are needed to meet clinical stiffness requirements, which is not a fundamental limitation. Also, the laboratory prototype was designed at twice the scale of the clinical system to accommodate the relatively large size of the hand fabricated actuators. Appropriate actuator manufacturing techniques that will relax these limitations are currently under development.

A three-dimensional position sensor is used to measure the needle motion (miniBird model 800, Ascension Technology Corp, Milton, VT). The device is an electromagnetic tracker and it can measure the position and orientation (6 DOF), with RMS precisions of 1.8 mm and 0.5°. The moving sensor has OD 1.3 mm; length 6.5 mm and 90 Hz data rate. The sensor is mounted on the needle tip as shown in Fig. 10.

The MRI compatibility of the device was verified in a 3 Tesla clinical MRI scanner (GE Healthcare, Milwaukee, WI). Methods outlined by Tsekos et al. [35] were used in the MRI compatibility assessment.

7. EXPERIMENTAL RESULTS

7.1 Workspace Kinematics

The workspace kinematics was studied on 54 input points selected randomly from the 4096 possible inputs (Fig. 11). The dashed circle shows the size of the required workspace for prostate detection and treatment. The solid line circle shows the size of average prostate. The size of the workspace is essentially the same as that predicted by the analysis.

Analytical results and experimental measurements are compared in Fig. 12. The circle shows the size of an average prostate. In this area, the average distance between the analytical predictions and experimental points is about 3mm. It should be noted that the miniBird sensor used in this experiment has an RMS error of about 1.4mm suggesting that more precise laser measurements and calibration currently underway will significantly reduce the measured experimental errors.

The positional error can be caused by unaccounted external forces and variations in manipulator parameters, e.g. dimensional and geometric tolerances, spring constants, and actuator strokes. In a production environment, DEAs forces and thus system stiffness would be high enough to neglect external forces. Variations in manipulator parameters should also be relatively small with appropriate manufacturing techniques. In the case of the laboratory prototype, there are no external forces but there are relatively important variations in manipulator parameters. Variations in actuator stroke and spring constant were estimated. Figure 13 compares the analytical results of this estimation with some experimental points taken from Fig. 11. The parameters were modified by adding error terms:

$$\begin{aligned} k_i &= k_{0i} + \Delta k_i \\ \xi_i &= \xi_{0i} + \Delta \xi_i \end{aligned} \qquad (13)$$

where the nominal value of the i^{th} spring constant and actuator stroke are k_{0i} and ξ_{0i}. The modified spring constant and actuator stroke were replaced in Eq.(9) leading to:

$$Ue' + \Delta Ue' = \frac{1}{\sum_i (k_{0i} + \Delta k_i)} \sum_i \Big[(k_{0i} + \Delta k_i) \ \ldots \qquad (14)$$

$$\ldots \ \{ l_{0i} + \Delta i + a_i (\xi_{0i} + \Delta \xi_i) \} W_i - l_{0i} V_i \Big]$$

Measurements show that the variation in the spring constant is about ±10% of the nominal value and the variation of the actuator stroke is about ±1.5mm. Such unusually large errors would be significantly reduced by better control of the mechanical stops in the bistable actuators and better materials for the springs. As shown in Fig. 13 by the error ellipses, the experimental dots are included between the minimum and maximum analytical errors. Hence the variation between the experimentally measured workspace and analytical predictions is likely due to variations in spring constant and actuator stroke. Also shown in Fig. 13, the errors due to parameters variation increase in the outermost portion of the

workspace. The error is actually quite small in the central portion of the workspace, in the area of the size of the average prostate.

The results presented here show that, even if there is some error, the experimental results are still reasonably inline with the model predictions. Further, the error would be significantly reduced through better manufacturing techniques. Therefore, it is reasonable to think that in a production environment, the experimental positioning accuracy would follow the model predicted positioning accuracy discussed in section 5.

7.2 MRI Compatibility

The DEAs used in the compatibility tests contain small amounts of materials that may affect image quality such as aluminum threaded rods and traces of nickel paint (ferromagnetic metal). The possible effect is disruption of the homogeneous magnetic field, causing image distortion or signal drop out. An image was acquired before introducing the DEA to serve as a baseline. A single plane of the DEA device with three bistable modules was positioned and images acquired. The baseline image was subtracted from images acquired with the DEA in place in order to assess this susceptibility artifact.

The effect of electromagnetic interference emitted from the DEA was also evaluated. A baseline image of a homogeneous phantom was acquired. The pixel value mean of a large region of interest inside the phantom was used as a metric of the signal. Next the radiofrequency transmitter was turned off in order to acquire images of only the noise. Images were acquired with the DEA in place, under various conditions. The standard deviation over the same region of interest was taken as a metric of the noise. Signal to noise ratio (SNR) was calculated by dividing the signal mean by the noise standard deviation.

Fig. 14 shows sagittal images acquired to assess susceptibility artifact. The device is positioned, but not visible, on the left side of the image. Images from left to write are (1) baseline conditions, (2) with the device in its working location with all actuators turned on and (3) with the device touching the phantom with all actuators turned on simultaneously (worst case scenario). No distortion was noted due to the presence of the DEA device. Although a materials substitution to materials such as plastics and silver (diamagnetic) paint could be done to reduce artifact, no change is merited.

To assess the impact of the device on the SNR of the images, images were acquired with (1) baseline conditions, with the device in its use case location (2) with the power supply off, (3) with the power supply on but not actuating, and (4) with all DEAs actuated. A 29% decrease in signal to noise ratio was noted during actuation, whereas only a 1% reduction was noted with the power supply on but not actuating. There has been no effort to filter the lines between the power supply and DEAs. The interference observed when the actuators are turned on would cause minimal problems since the bistable approach the actuators maintain their states without power, and the necessary application of power to change states in transient. The tests on the assembled system confirmed previous results on individual actuators showing DEAs to be MRI compatible [7,8].

8. CONCLUSION

This paper shows that the proposed parallel manipulator concept based on elastically averaged bistable DEAs is a promising approach to target prostrate cancer in patients located within the aperture of a closed-bore high field clinical MRI scanner. Manipulator positioning accuracy is shown to meet the clinical design criteria both analytically and empirically. MRI compatibility is successfully verified at 3 Tesla.

More work is needed to bring the parallel manipulator concept presented here to a clinical device. In particular, DEA manufacturing techniques must improve to reduce positioning errors, decrease size, and increase system stiffness. An automated fabrication process for small, high force DEAs using multiple polymer layers is currently under development. Also, manipulator control during needle insertion remains to be studied.

The manipulation approach proposed in this paper could lead to the development of simple and low cost mechatronic devices that could have a significant impact on MRI-guided medical interventions to prostate cancer, breast and other cancers within the thorax, abdomen, and pelvis, endovascular interventions, and spinal procedures.

ACKNOWLEDGEMENTS

The valuable inputs from Dr. Clare Tempany in the preparation of this work are acknowledged and truly appreciated. This work was supported in part by The Massachusetts Institute of Technology (MIT), The NASA Institute for Advanced Concepts (NIAC), The Center for Integration of Medicine and Innovative Technology (CIMIT), and the Cambridge-MIT Institute (CMI). D.F. Kacher, S.P. DiMaio, and F.A. Jolesz were funded by NIH 1U41RR019703-01A2. J.R. Roebuck was funded by NIH 5R25-CA089017.

LISTE OF FIGURES

FIGURES

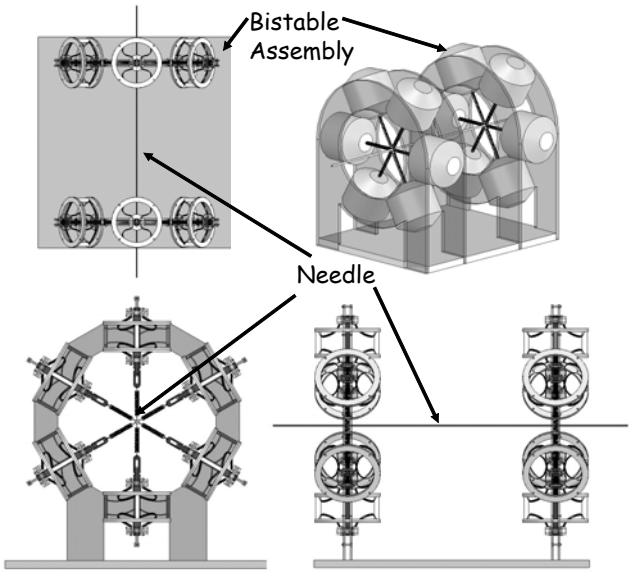

(a) System Concept

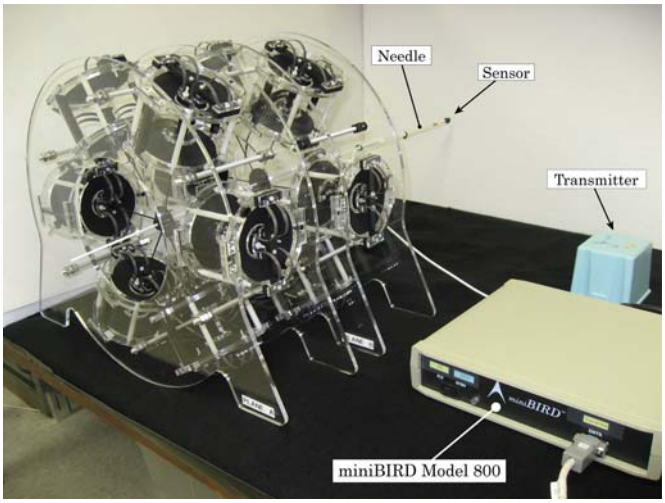

(b) Experimental System

Fig. 1. A laboratory prototype MRI manipulator.

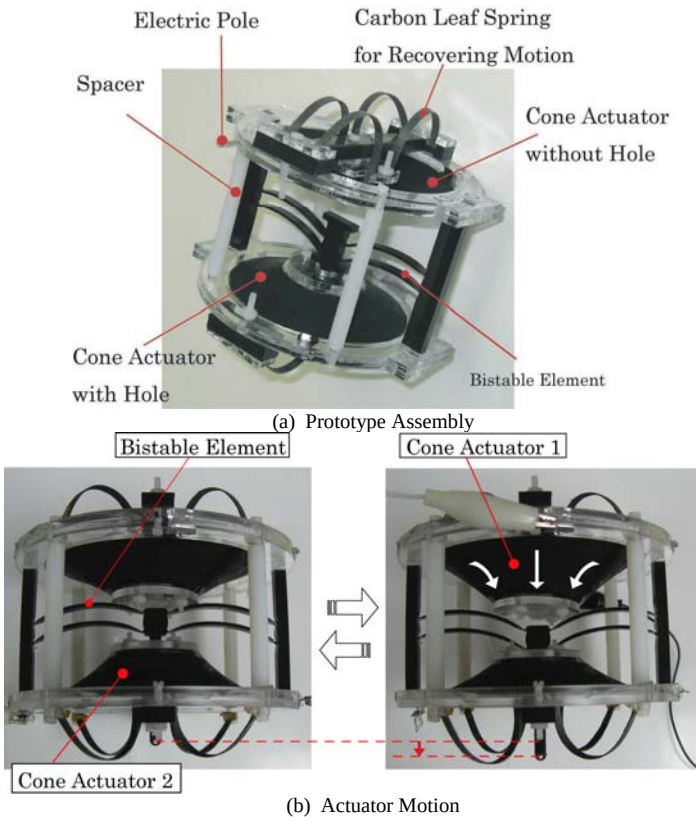

Fig. 2. A bistable module assembly using antagonistic DEAs.

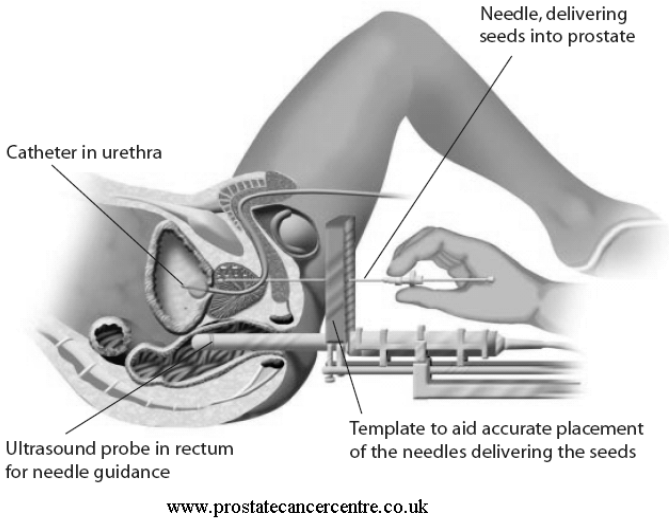

Fig. 3. Transperineal brachytherapy procedure.

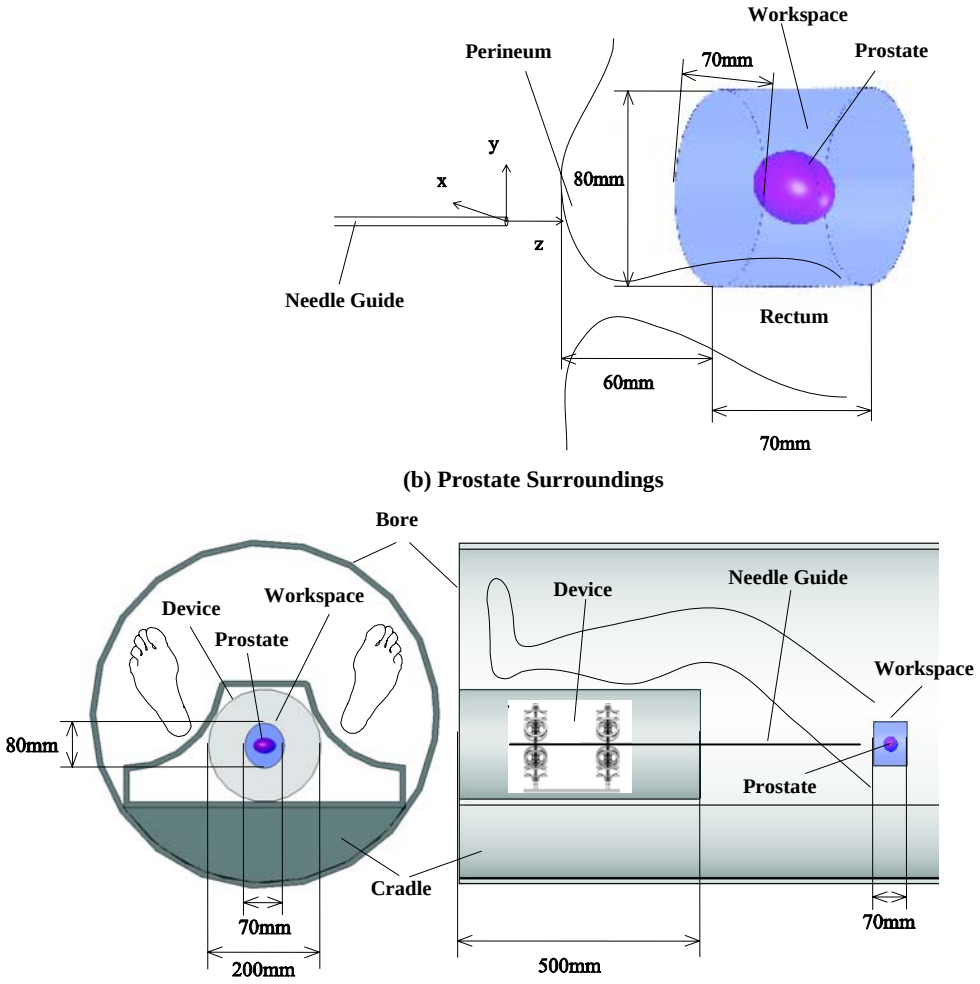

Fig. 4: Workspace and manipulator size constraints.

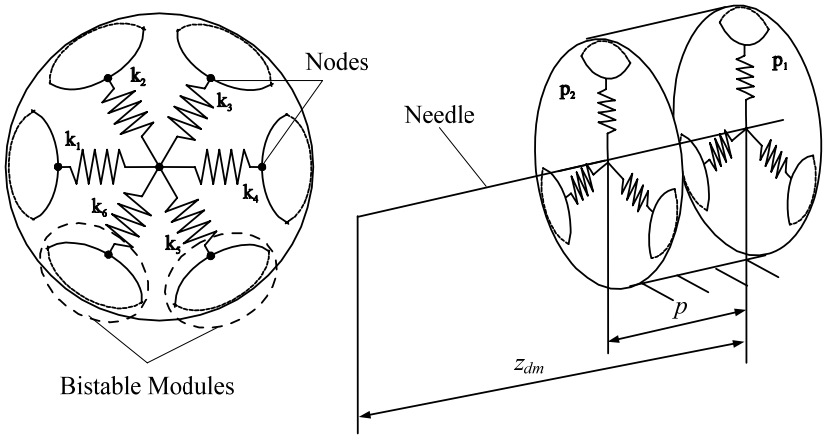

(a) One Plane of Device. (b) Two Plane Assembly

Fig. 5 Schematic of proposed manipulator.

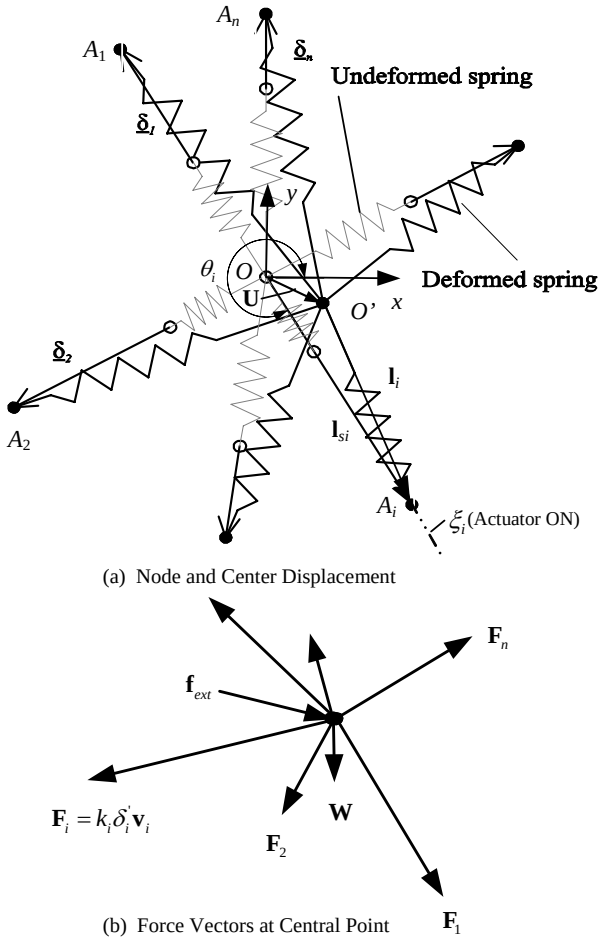

Fig. 6. Actuation center point free-body diagrams.

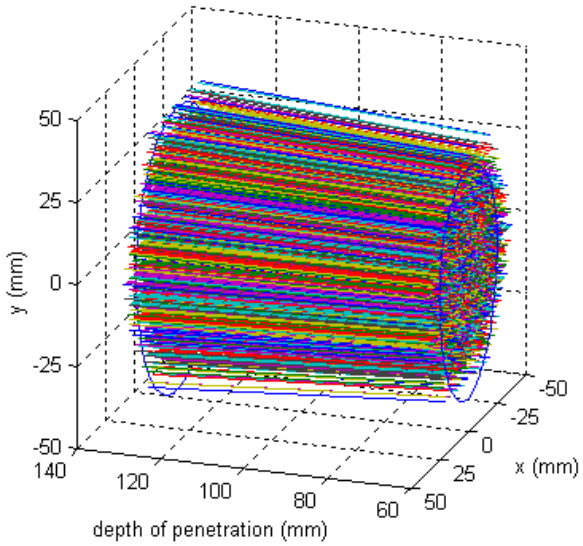

(a) Needle Workspace

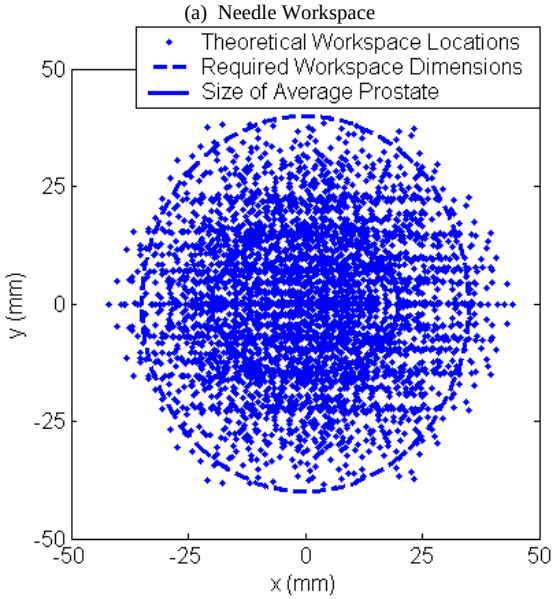

(b) Workspace at Insertion Depth of 110mm

Fig. 7. Analytically Predicted Workspace of MRI the Manipulator.

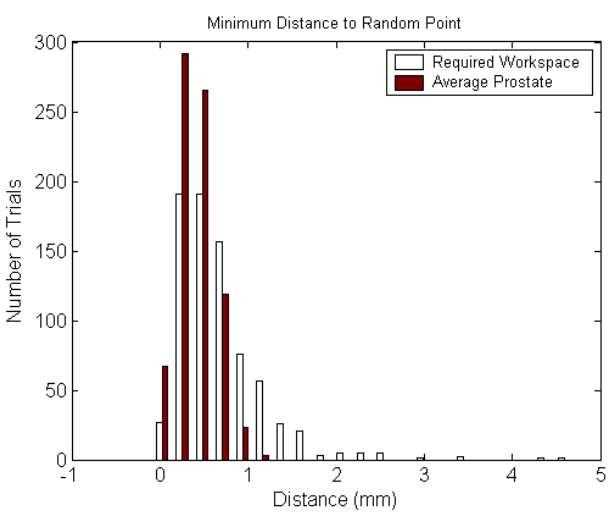

Fig. 8. Minimum distances from a reachable end effector point to random target location**.**

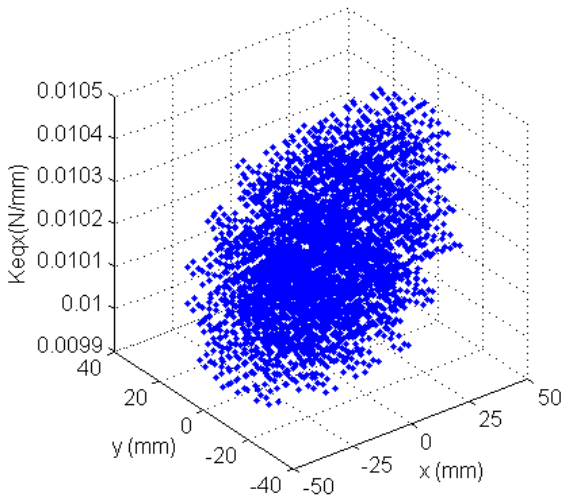

Fig.9. Distribution of system stiffness at 110mm beyond perineum wall**.**

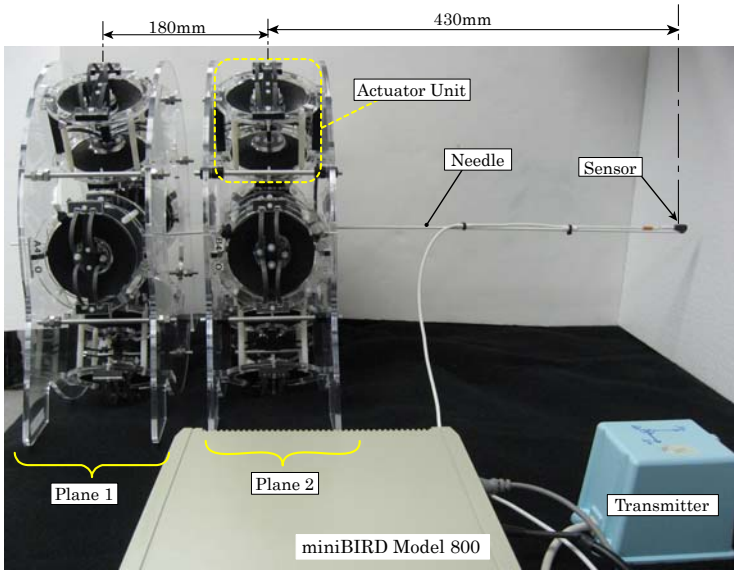

Fig. 10. Manipulator and the measuring device.

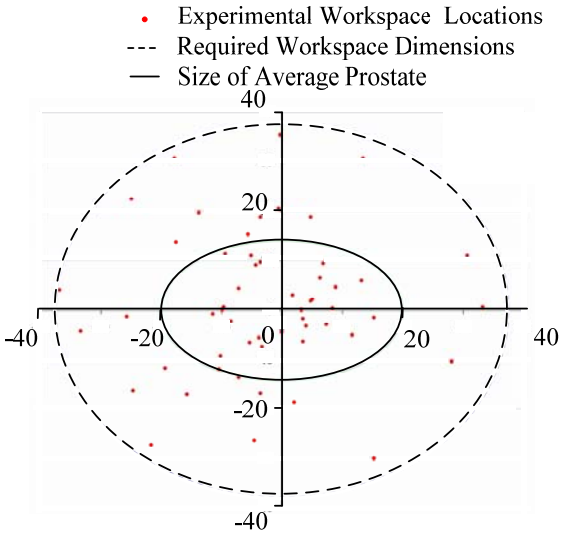

Fig. 11. Needle experimental workspace (units in mm).

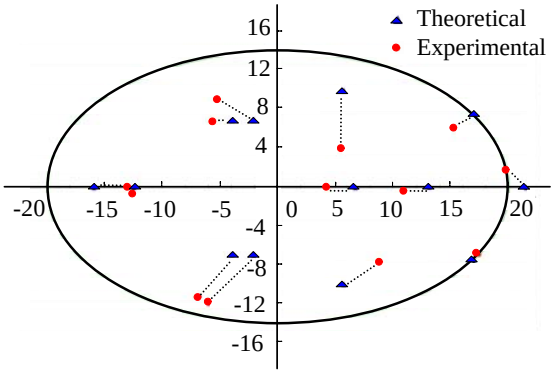

Fig.12. Needle placement performance in the prostate workspace (units in mm).

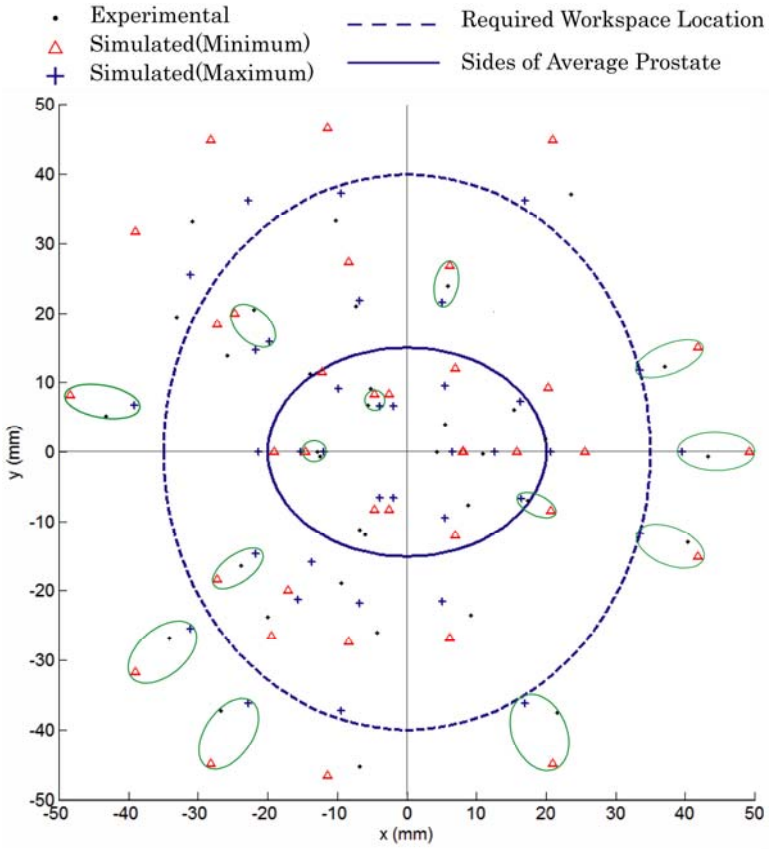

Fig. 13. Needle experimental and analytical plots.

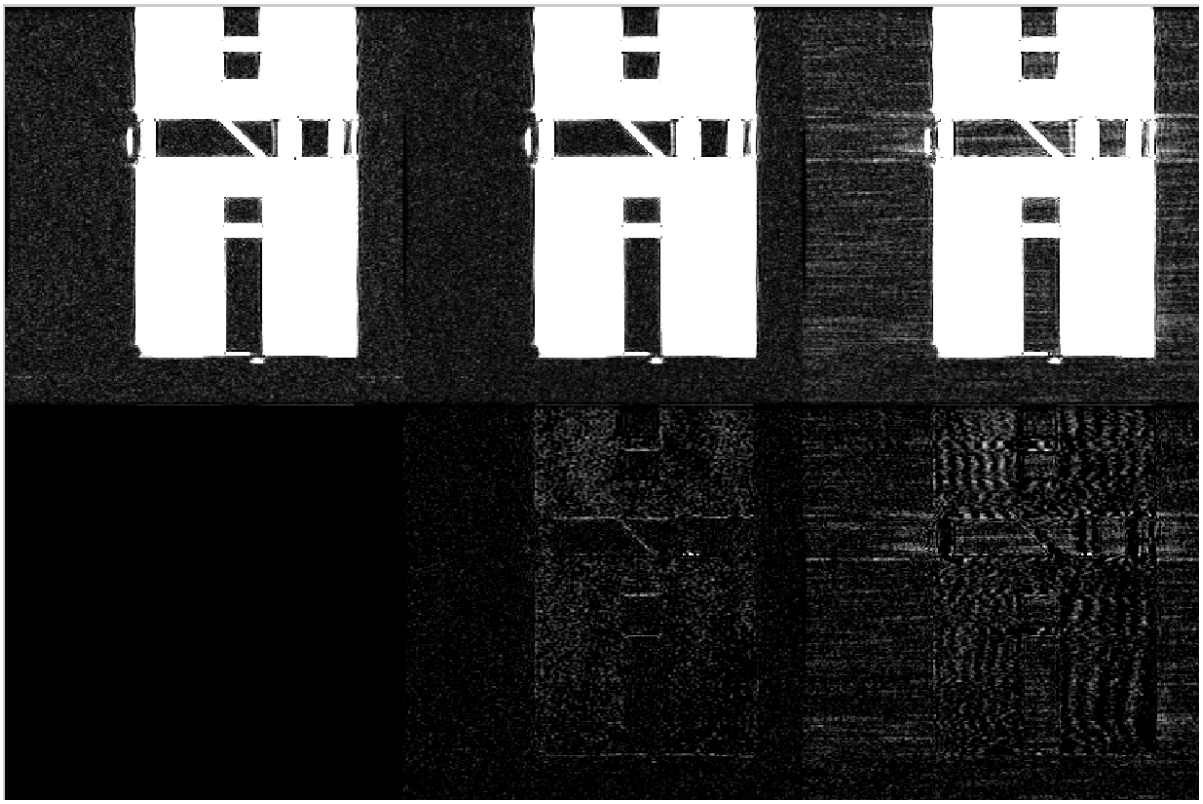

Fig. 14. Susceptibility artifact assessment. **Top:** from left to right: baseline, DEAs actuating with device in use-case location, DEAs actuating with device touching phantom. **Bottom:** the baseline image subtracted from the top images. No distortion to the left side of the phantom, which is in proximity to the device, is noted. The horizontal lines in the top right image are due to electromagnetic interference, not susceptibility.

TABLES

Table I. Manipulator Parameters (mm)

p	l_{oi}	ξ_i	z_{dm}
180	86	13	560/630

Table II. Spring Constants, k=0.044 N/mm

	k_1	k_2	k_3	k_4	k_5	k_6
Plane 1	*3k/2*	*k*/2	*k*	*k*/2	*k*	*k*/2
Plane 2	*k*/2	*k*	*k*/2	*k*/2	*k*/2	*k*

Table III. Parameters of an Actuator Plane Module

Outer Radius	200mm
Inner diameter	175mm
Width	17mm
Weight	2.75kg
Weight (actuator unit)	(104g)

REFERENCES

[1] Hafez, M., Lichter, M., and Dubowsky, S., 2003, "Optimized Binary Modular Reconfigurable Robotic Devices," IEEE/ASME Transactions on Mechatronics, **8**, pp.18-26.

[2] DeVita, L.M., Plante, J.S., and Dubowsky, S., 2007, "The Design of High Precision Parallel Mechanisms using Binary Actuation and Elastic Averaging: With Application to MRI Cancer Treatment," *Proceeding of the 2007 IFToMM World Congress on Machines and Mechanisms*, Besançon, France, pp.17-21.

[3] Chirikjian, G.S., 1997, "Inverse Kinematics of Binary Manipulators Using a Continuum Model," Journal of Intelligent and Robotic Systems, **19**, pp.5–22

[4] Sujan, V., Lichter, M., and Dubowsky S., 2001, "Lightweight Hyper-redundant Binary Elements for Planetary Exploration Robots," *Proc. 2001 Int. Conf. on Advanced Intel. Mechatronics*, Como, Italy, July.

[5] Plante, J.S., Santer, M., and Dubowsky, S., Pellegrino, S., 2005, "Compliant Bistable Dielectric Elastomer Actuators for Binary Mechatronic Systems," *Proc. of the 2005 ASME Mechanism and Robotics Conference*, Long Beach, CA, September.

[6] Plante, J.S., and Dubowsky, S., 2006, "Large-Scale Failure Modes of Dielectric Elastomer Actuators," The International Journal of Solids and Structures, **43**, pp.7727-7751.

[7] Kacher, D.F., Vogan, J., Wingert, A., Hafez, M., Plante, J.S., Dubowsky, S., and Jolesz, F.A., 2004, "Development of a Reconfigurable MRI Coil using Electrostrictive Polymer Artificial Muscle Actuators," *Proc of the Int. Soc. of Magnetic Resonance in Medicine*, Kyoto, May.

[8] Vogan, J., Kacher, D., Wingert, A., Hafez, M., Plante, J.S., Jolesz, F., and Dubowsky, S., 2004, "Manipulation in MRI Devices using Electrostrictive Polymer Actuators: With an Application to Reconfigurable Imaging Coils". *Proc. IEEE ICRA*, New Orleans, April.

[9] Slocum, A., 1992, *Precision Machine Design*. Society of Manufacturing Engineers.

[10] Jemal, A., Murray, T., Ward, E., Samuels, A., Tiwari, R.C., Ghafoor, A., Feuer, E.J., and Thun, M.J., 2005, Cancer Statistics, 2005. C.A.: A Cancer Journal for Clinicians, **55**, (1), pp.10-30.

[11] American Cancer Society. 2007, *Cancer facts and figures 2007*. American Cancer Society; Atlanta.

[12] Wilson, S., Tesoro, R., Elkin, E.P., Sadetsky, N., Broering, M., Latini, D.M., Duchane, J., Mody, R.R., and Carroll, P.R., 2007, "Cumulative Cost Pattern Comparison of Prostate Cancer Treatments", Cancer, **109**, (3), pp.518-527.

[13] Jolesz, F., 2005, "Future perspectives for intraoperative MRI," Neurosurgery Clinics of North America, **16**, pp.201-213.

[14] Nag, S., Beyer, D., Friedland, J., Grimm, P., and Nath, R., 1999, "American Brachytherapy Society (ABS) Recommendations for Transperineal Permanent Brachytherapy of Prostate Cancer," Intern. Jour. of Radiation Oncology Biology Physics, **44**, (4), pp.789-799.

[15] D'Amico, A., Tempany, C., Cormack, R., Hata, N., Jinzaki, M., Tuncali, K., Weinstein, M., and Richie, J., 2000, "Transperineal magnetic resonance image guided prostate biopsy,".J Urol., **164**, (2), pp.385-387.

[16] D'Amico, A., Cormack, R., Kumar, S., and Tempany, C.M., 2000, "Real-time magnetic resonance imaging-guided brachytherapy in the treatment of selected patients with clinically localized prostate cancer," J Endourol., **14**, (4), pp.367-370.

[17] Krieger, A., Csoma, C., Iordachital, I.I., Guion, P., Singh, A.K., Fichtinger, G., and Whitcomb, L.L., 2007, "Design and preliminary accuracy studies of an MRI-guided transrectal prostate intervention system," *Med Image Comput Comput Assist Interv Int Conf Med Image Comput Comput Assist Interv*, **10,** (Pt 2):59-67.

[18] Krieger, A., Susil, R.C., Ménard, C., Coleman, J.A., Fichtinger, G., Atalar, E., and Whitcomb, L.L., 2005, "Design of a novel MRI compatible manipulator for image guided prostate interventions," IEEE Trans Biomed Eng., **52**, (2), pp.306-313.

[19] Susil, R.C., Ménard, C., Krieger, A., Coleman, J.A., Camphausen, K., Choyke, P., Fichtinger, G., Whitcomb, L.L., Coleman, C.N., and Atalar, E., 2006, "," J Urol., **175,** (1), pp.113-20.

[20] Fischer, G.S., Iordachita, I., DiMaio, S.P., and Fichtinger, G., 2007, "Development of a Robotic Assistant for Needle-Based Transperineal Prostate Interventions in MRI," *10th International Conference on Medical Image Computing and Computer-Assisted Intervention - MICCAI 2007*, Brisbane, Australia, **1**, pp.425-453.

[21] Mewes, P.W., Tokuda, J., DiMaio, S.P., Fischer, G.S., Csoma, C., Gobbi, D.G., Tempany, C.M., Fichtinger, G., and Hata, N., 2008, "An Integrated MRI and Robot Control Software for an MRI-compatible Robot in Prostate Intervention," *International Conference on Robotics and Automation - ICRA 2008*, Pasadena, CA.

[22] Fischer, G.S., Iordachita, I., Csoma, C., Tokuda, J., Mewes, P.W., Tempany, C.M., Hata, N., and Fichtinger, G., 2008, "Pneumatically Operated MRI-Compatible Needle Placement Robot for Prostate Interventions," *International Conference on Robotics and Automation - ICRA 2008*, Pasadena, CA.

[23] Tokuda, J., DiMaio, S.P., Fischer, G.S., Csoma, C., Gobbi, D., Fichtinger, G., Hata, N., and Tempany, C.M., 2008, "Real-time MR Imaging Controlled by Transperineal Needle Placement Device for MRI-guided Prostate Biopsy," *16th Scientific Meeting and Exhibition of the International Society of Magnetic Resonance in Medicine - ISMRM 2008*, Toronto, Canada.

[24] Fischer, G.S., Iordachita, I., Csoma, C., Tokuda, J., DiMaio, S.P., Tempany, C.M., Hata, N., and Fichtinger, G., 2008 "MRI-Compatible Pneumatic Robot for Transperineal Prostate Needle Placement," IEEE / ASME Transactions on Mechatronics – Focused Section on MRI Compatible Mechatronic Systems.

[25] Fischer, G.S., DiMaio, S.P., Iordachita, I.I., and Fichtinger, G., 2007, "Robotic assistant for transperineal prostate interventions in 3T closed MRI," *Med Image Comput Comput Assist Interv Int Conf Med Image Comput Comput Assist Interv.*, **10**, (Pt 1), pp.425-433.

[26] Patriciu, A., Petrisor, D., Muntener, M., Mazilu, D., Schär, M., and Stoianovici, D., 2007, "Automatic brachytherapy seed placement under MRI guidance," IEEE Trans Biomed Eng., **54**, (8), pp.1499-1506.

[27] Larson, B.T., Erdman, A.G., Tsekos, N.V., Yacoub, E., Tsekos, P.V., and Koutlas, I.G., 2004, "Design of an MRI-compatible robotic stereotactic device for minimally invasive interventions in the breast," J Biomech Eng., **126**, (4), pp.458-465.

[28] Melzer, A., Gutmann, B., Remmele, T., Wolf, R., Lukoscheck, A., Bock, M., Bardenheuer, H., and Fischer, H., 2008, "INNOMOTION for percutaneous image-guided interventions: principles and evaluation of this MR- and CT-compatible robotic system," IEEE Eng Med Biol Mag., **27**, (3), pp.66-73

[29] Tsekos, N.V., Christoforou, E., and Ozcan, A., 2008, "A general-purpose MR-compatible robotic system: implementation and image guidance for performing minimally invasive interventions," IEEE Eng Med Biol Mag., **27**, (3), pp.51-58.

[30] DiMaio, S., Pieper, S., Chinzei, K., Hata, N., Haker, S., Kacher, D., Fichtinger, G., Tempany, C., and Kikinis, R., 2007, "Robot-assisted needle placement in open MRI: system architecture, integration and validation," Comput Aided Surg., **12**, (1), pp.15-24.

[31] Koseki, Y., Koyachi, K., Arai, T., and Chinzei, K., 2003, "Remote Actuation Mechanism for MR-compatible Manipulator Using Leverage and Parallelogram -Workspace Analysis, Workspace Control, and Stiffness Evaluation", *Proc. of ICRA2003*, pp. 652-657.

[32] Koseki, Y., Kikinis, R., Jolesz, F., and Chinzei, K., 2004, "Precise Evaluation of Positioning Repeatability of MR-Compatible Manipulator Inside MRI," *Medical Image Computing and Computer-Assisted Intervention*, Saint-Malo, France, September 26-30, pp. 192-199.

[33] Gassert, R., Burdet, E., and Chinzei, K., 2008, "Opportunities and challenges in MR-compatible robotics: reviewing the history, mechatronic components, and future directions of this technology," IEEE Eng Med Biol Mag., **27**, (3), pp.15-22.

[34] Gassert, R., Burdet, E., and Chinzei, K., 2008, "MRI-Compatible Robotics," IEEE Eng Med Biol Mag., **27**, (3), pp.12-14.

[35] Tsekos ,N.V., Khanicheh, A., Christoforou, E., and Mavroidis, C., 2007, "Magnetic resonance-compatible robotic and mechatronics systems for image-guided interventions and rehabilitation: a review study," Annu Rev Biomed Eng., **9**, pp.351-387.

[36] Blumenfeld, P., Hata, N., Dimaio, S., Zou, K., Haker, S., Fichtinger, G., and Tempany C, 2007, "Transperineal prostate biopsy under magnetic resonance image guidance: A needle placement accuracy study," J Magn Reson Imaging. **26**, (3), pp.688-694.

[37] DiMaio, S.P., and Salcudean, S.E., 2005, "Needle steering and motion planning in soft tissues", IEEE Trans. Biomed Eng., **52**, (6), pp. 965-974.

[38] Chinzei, K., and Miller, K., 2001, "Towards MRI guided surgical manipulator," Med Sci Monit, **7**, (1), pp.153-163.

[39] Wendt, O., Oellinger, J., Luth, T.C., Felix, R., and Boenick, U., 2000, "The effects of the use of piezoelectric motors in a 1.5-Tesla high-field magnetic resonance imaging system (MRI)," Biomed. Tech., **45**, pp.20-25.

[40] Taillant, E., Avila-Vilchis, J.C., Allegrini, C., Bricault, I., and Cinquin, P., 2004, "CT and MR Compatible Light Puncture Robot: Architectural Design and First Experiment," *Medical Image Computing and Computer-Assisted Intervention*, Saint-Malo, France, pp.145-152.

[41] DiMaio, S.P., Fisher, G.S., Haker, S.J., Hata, N., Iordachita, I., Tempany, C.M., Kikinis, R., and Fichtinger, G., 2006, "A Sytem for MRI-guided Prostate Interventions," *International Conference on Biomedical Robotics and Biomechatronics*, Pisa, Italy, Febuary, pp.68-73.

[42] Stoianovici, D., Patriciu, A., Petrisor, D., Mazilu, D., and Kavoussi, L., 2007, "A New Type of Motor: Pneumatic Step Motor," IEEE/ASME Transactions on Mechatronics, **12**, pp.98-106.

[43] Devita, L., 2007, "An MRI Compatible Manipulator for Prostate Cancer Detection and Treatment," MS Thesis, Massachusetts Institute of Technology, Cambridge.